

# The Bi-directional Moving Structures in a Coronal Bright Point

Dong Li<sup>1,2</sup> & Zongjun Ning<sup>1</sup> & Yingna Su<sup>1</sup>

lidong@pmo.ac.cn  
ningzongjun@pmo.ac.cn  
ynsu@pmo.ac.cn

## ABSTRACT

We report the bi-directional moving structures in a coronal bright point (CBP) on 2015 July 14. It is observed by the Atmospheric Imaging Assembly (AIA) onboard *Solar Dynamics Observatory* (SDO). This CBP has a lifetime of  $\sim 10$  minutes, and a curved shape. The observations show that many bright structures are moving intermittently outward from the CBP brightness core. Such moving structures are clearly seen at AIA 171 Å, 193 Å, 211 Å, 131 Å, 94 Å, 335 Å and 304 Å, slit-jaw (SJI) 1330 Å and 1400 Å. In order to analyze these moving structures, the CBP is cut along the moving direction with a curved slit from the AIA and SJI images. Then we can obtain the time-distance slices, including the intensity and intensity-derivative diagrams, from which, the moving structures are recognized as the oblique streaks, and they are characterized by the bi-direction, simultaneity, symmetry, and periodicity. The average speed is around  $300 \text{ km s}^{-1}$ , while the typically period is  $\sim 90 \text{ s}$ . All these features (including the bi-directional flows and their periodicity) can be detected simultaneously at all the 9 wavelengths. This CBP takes place at the site between a small pair of magnetic polarities. High time resolution observations show that they are moving close to each other during its lifetime. These facts support the magnetic reconnection model of the CBP and the bi-directional moving structures could be the observational outflows after the reconnection. Therefore, they can be as the direct observation evidence of the magnetic reconnection.

*Subject headings:* Sun: atmosphere; Sun: UV radiation; Sun: magnetic reconnection

## 1. Introduction

Bright points (BPs) are frequently detected as the small scale brightness enhancements on solar disk. Different from the larger scale solar burst phenomena, i.e., flares and CMEs, they are very common phenomena in the active regions, quiet Sun or even coronal holes. The BPs are usually observed at the solar atmosphere, i.e., from photosphere through chromosphere to corona. The BPs observed at X-rays (Zhang et al. 2012; Zhang & Ji 2013; Zhang et al.

2014), extreme ultraviolet (EUV) (Ning & Guo 2014; Alipour & Safari 2015), and ultraviolet (UV) (Li & Ning 2012; Li et al. 2013) bands are generally called coronal bright points (CBPs). They usually display the small roundish or loop-shaped features. The CBPs have a typical size of about  $5\text{--}40''$ , and they can last for a few hours or longer (Vaiana et al. 1973; Golub et al. 1974). Statistical results indicate that about 1500 CBPs emergence at the full solar surface every day (Golub et al. 1974). And further studies suggest that there are 800 CBPs emergence on the entire solar surface at any given time (Zhang et al. 2001). Therefore, they are thought to be contributed to the coronal heating. However, the number and distribution of the CBPs on solar atmospheres are different between solar maximum and minimum years. In other words, there are

<sup>1</sup>Key Laboratory of Dark Matter and Space Astronomy, Purple Mountain Observatory, CAS, Nanjing 210008, China

<sup>2</sup>Key Laboratory of Modern Astronomy and Astrophysics (Nanjing University), Ministry of Education, Nanjing 210093, China

much more CBPs emergence at sunspot minimum than that at sunspot maximum, and they appear more uniformly during solar minimum over the solar surface. The number of the CBPs becomes less when their lifetimes are longer (Priest et al. 1994). On the other hands, previous studies have found that the temperature of the CBPs is about several MK, while their electron density has an order of  $\sim 10^9 \text{ cm}^{-3}$ , which corresponds to the emission measure (EM) of about  $10^{27} \text{ cm}^{-5}$  (Nolte et al. 1979; Tian et al. 2008a; Kariyappa et al. 2011; Hong et al. 2014; Zhang et al. 2014).

The CBPs are usually believed to be the results of the small-scale magnetic reconnection (Priest et al. 1994; Zhang et al. 2012; Innes & Teriaca 2013). Observations show that the CBPs are always associated with the small-scale magnetic fields which have opposite-polarity poles (Golub et al. 1976; Li & Ning 2012). And these small magnetic fields are always new emergence and have the fluxes of about  $10^{18} - 10^{19} \text{ Mx}$  (Priest et al. 1994; Li et al. 2013). Previous findings further indicated that one third of the CBPs occur at the new ephemeral magnetic regions, whereas the other two thirds of them are lied above the cancelations of the opposite-polarity magnetic fields (Harvey 1985; Webb et al. 1993). Using the observations with high time resolution, several authors have investigated the relationship between the CBPs and the moving behaviors of magnetic fields (or the change of the magnetic flux) (e.g., Harvey et al. 1994; Alexander et al. 2011; Li & Ning 2012; Zhang et al. 2012; Chen et al. 2015). They found that the CBP is associated with magnetic cancellation. All these findings support the magnetic reconnection model for the CBPs. Based on the 2-D reconnection model (Sturrock & Coppi 1964), the bi-directional outflows can be produced simultaneously, and the radiation along their propagation path could be observed at EUV or optical wavelengths. For example, the bi-directional outflows are well detected in the transition-region explosive events (Innes et al. 1997; Pérez et al. 1999; Innes & Teriaca 2013; Innes et al. 2015) and solar flares (Su et al. 2013; Liu et al. 2013; Ning 2016). The reconnections flows are called as the downflows and upflows according to the moving directions (toward or away) from the solar surface.

Similar as the quasi-periodic oscillations in

the solar flare (Li et al. 2015; Ning 2016), some CBPs also display the quasi-periodic oscillations, such as the periodic variation in intensity and Doppler shifts at X-ray and EUV bands (Nolte et al. 1979; Tian et al. 2008b; Zhang & Ji 2014a; Samanta et al. 2015), or the repeated bi-directional flows at EUV bands (Ning & Guo 2014). The periods of these oscillations are ranging from seconds to tens of minutes. For example, Ning & Guo (2014) detected the quasi-periods between 80 and 100 s at 9 AIA EUV (or UV) bands in a curved CBP. While Tian et al. (2008b) found the intensity oscillations with long periods ranging from 8 to 64 min in the CBPs. Recently, Samanta et al. (2015) found the correlation between the imaging intensity and the spectral line parameters in a CBP. All these findings suggest that the quasi-periodic oscillations in the CBP could be explained by the repetitive and small-scale magnetic reconnections on the solar surface (Priest et al. 1994; Zhang et al. 2014; Chen et al. 2015; Samanta et al. 2015). And the observed period could be the same as that of the modulated MHD waves (e.g., Chen & Priest 2006; Banerjee & Krishna Prasad 2016). This is also consistent well with the 2-D reconnection model (Sturrock & Coppi 1964).

Using the observations from SOHO/SUMER (Wilhelm et al. 1997), the studies of the bi-directional outflows had been breakthrough. However, these phenomena are mostly in the short-time scale, such as explosive events (e.g., Innes et al. 1997; Pérez et al. 1999; Innes & Teriaca 2013), chromospheric upflow events (Chae et al. 1998), and blinkers (Chae et al. 2000; Brković & Peter 2004; Bewsher et al. 2005). Following the observation results, the MHD simulations is applied to build up the models of these events based on the magnetic reconnection (see., Innes & Tóth 1999; Sarro et al. 1999; Roussev et al. 2001a,b). Until now, investigation on the bi-directional outflows in the CBP is still poorly done. In this paper, using the multi-wavelength observations from the slit-jaw (SJI) aboard *Interface Region Imaging Spectrograph (IRIS)*, the Atmospheric Imaging Assembly (AIA) and Helioseismic and Magnetic Images (HMI) on board *Solar Dynamics Observatory (SDO)*, we explore the bi-directional outflows and their generation in a CBP at multi-wavelengths with high spatial and temporal resolution data.

## 2. Observations

The CBP studied here takes place in NOAA AR12384 on July 14 2015. It starts at about 01:00 UT and reaches its maximum at around 01:06 UT. Fig. 1 (left) shows the  $H\alpha$  6563 Å image observed by NSO/GONG at 01:04:54 UT which is close to the peak time of the CBP. There is no data between 01:05 and 01:11 UT for the NSO/GONG at  $H\alpha$  6563 Å. The contours represent the magnetic fields from *SDO*/HMI (Schou et al. 2012), and the levels are set at 200 (purple) and -200 (green) Gauss, respectively. The blue box marks the region where the CBP takes place, and it is about  $40'' \times 40''$ . The CBP starts at the position of  $x=-36.5''$ ,  $y=-440.8''$ , as marked by the red plus.

*SDO*/AIA (Lemen et al. 2012) can observe the full solar disk with a spatial scale of  $\sim 0.6''$  per pixel at seven EUV and two UV channels. The time cadence is 12 s at EUV channels, while 24 s at UV channels. Fig. 2 presents the AIA images at all 9 wavelengths, such as 171 Å, 193 Å, 211 Å, 335 Å, 131 Å, 94 Å, 304 Å, 1600 Å and 1700 Å, and the *IRIS*/slit-jaw (SJI) (De Pontieu et al. 2014) images at three wavelengths, such as SJI 1330 Å, 1400 Å and 2796 Å. SJI observations have a cadence of about 20 s and a field view of about  $40'' \times 40''$ , as shown by the blue box marked in Fig. 1. The SJI images missed the data at the bottom. The CBP is bright at 7 AIA EUV and 2 SJI FUV bands, and it is very weak at AIA 1600 Å, 1700 Å and SJI 2796 Å.

## 3. Data Reduction

As mentioned above, both *SDO*/AIA and *IRIS*/SJI have high time resolution, which gives us an opportunity to study the evolution of this CBP in detail. Fig. 3 shows the time evolution of the CBP at AIA 171 Å. The top-half of the 18 panels display the intensity images from 01:04:46 UT to 01:08:10 UT, including the CBP maximum at  $\sim 01:06$  UT. There are some bright structures on these images. These structures are almost simultaneously moving outward from the CBP core (marked by the red plus in Figs. 1 and 2). For example, the purple arrows mark the two moving structures. They are moving away separately from the CBP core, one towards northwest, another towards southeast. Actually, all of the bright

structures are moving not along a straight path, but a curved way. Therefore, this CBP displays a curved shape in the images with high spatial resolution. These moving structures start with a bright patch, and their brightness decreases with the distance from the core, then disappear far from the core. The other 18 panels of Fig. 3 are the running-difference images at the same time interval. In these images, one moving structure is divided into one white and one dark kernels. The white kernel is followed by the dark one, and the positions of both kernels are changing simultaneously, as shown by the purple arrows.

Fig. 3 just displays the CBP evolution at AIA 171 Å. In order to display this CBP at other wavelengths, we plot the time-distance slices along an artificial slit following the curved shape of this CBP. Firstly, the slit is outlined along the curved shape with two white dashed lines, as shown in Figs. 2 and 3. Here we use a constant width of  $\sim 12''$  in order to cover the bulk of the CBP brightness as much as possible during its lifetime at various wavelengths. Secondly, the intensities between these two dashed curves are integrated. Thus, we can obtain the time-distance slices of the intensities at 7 AIA EUV bands and 2 SJI FUV channels, as shown in Fig. 4. The Y-axis is the artificial slit from southeast (bottom) to northwest (top). Thus, the middle of Y-axis, i.e.,  $\sim 20''$  is the core position of this CBP. This CBP begins to become bright at around 01:00 UT, then gradually expands, and significantly enhances almost simultaneously ( $\sim 01:04$  UT) at all the 9 wavelengths. The moving structures from the CBP core are identified as the oblique streaks on the time-distance slices. They are considered as the flows (e.g., Ning & Guo 2014). Some of them are moving upwards, some others are moving downwards, as indicated in Fig. 4. In order to detect these flows, the time derivative is calculated along the time axis on the time-distance slices. Fig. 5 shows the derivative time-distance slices at 9 wavelengths. The flows are still identified as the oblique streaks, which are shown clearly and each one is labeled by the arrow. In this case, one flow is divided into two streaks, a white streak followed by a dark one. Similar as the method used to study the thread in a prominence (Ning et al. 2009a,b), a pair of white and dark streaks here are consistent with the movement of a pair of white and

dark kernels on the running-difference images in Fig. 3. For example, a purple arrow marks one flow moving outward southeast, it corresponds to the oblique streak labeled by the purple arrow downward in Fig. 5, with a speed of about  $331 \text{ km s}^{-1}$ . Another purple arrow refers to the flow moving to northwest at the same time, it corresponds to another oblique streak marked by the purple arrow upward, with a speed of around  $234 \text{ km s}^{-1}$ . This pair of bi-directional flows are detected at all the 9 wavelengths, as indicated by the bi-directional purple arrows. We also find another pair of such bi-directional flows which are detected at all the 9 wavelengths, as shown by the pairs of blue arrows in Fig. 5. Both of these two pairs of bi-directional flows appear at the peak time of this CBP.

## 4. Results

### 4.1. The observational features

Figs. 4 and 5 show that the flows move upward (northwest) and downward (southeast) simultaneously. As marked by the bi-directional arrows, the flows appear with a pair, and they start from the CBP core (near about  $y=20''$ ). Meanwhile, a pair of the bi-directional flows have a similar speed. They are symmetrical on the time-distance slice. There are a number of bi-directional flows seen at AIA 171 Å, while some of them display very weak signature at AIA 94 Å and 335 Å. This indicates that these bi-directional flows tend to be bright at the upper chromosphere, transition region or the lower corona. The average moving velocity (speed) of these flows (including the upflows and downflows) is estimated to about  $300 \text{ km s}^{-1}$  here, and this value is similar to that in the outflows detected in the solar flares (see., Wang et al. 2007; Li & Zhang 2009; Liu et al. 2013; Su et al. 2013; Young et al. 2013; Ning 2016).

Except for these flows are bi-directional, simultaneous, and symmetrical, they are intermittently and exhibit the periodicity, whatever upward and downward flows. Fig. 6 (top panels) plots the light curves at the position marked by the purple line in Fig. 4. There are several subpeaks on these light curves at different wavelengths, and each subpeak indicates a flow. In order to study these subpeaks' periodicity, the light curve is decomposed into a slowly varying and a rapidly varying components. The slowly varying component is the smoothing

original flux, as shown by the blue dashed line overplotted on the light curve. Noting that the smoothing window is different for the data with different time resolution (see also., Li et al. 2015). For example, it is 10 points for AIA data ( $12 \text{ s} \times 10$ ) while 6 points for SJI data ( $20 \text{ s} \times 6$ ). The smoothing window has a same interval of 120 s for both data. The rapidly varying component is the light curve subtracted by the slowly varying component. Then the wavelet analysis is applied to detect the periods in the rapidly varying component. Fig. 6 presents the results at 9 wavelengths. Top panels show the light curves (solid) along the purple line in Fig. 4 and the blue dashed profiles are the slowly varying components. Middle panels display the rapidly varying components with plus signs. The wavelet spectra are shown at the bottom. A typical period of around 90 s are detected for all these 9 wavelengths, indicating that this CBP has the quasi-periodic oscillations, which is similar to the behaviors of quasi-periodic oscillations in the solar flares (Li et al. 2015; Ning 2016).

Using the same method, Fig. 7 displays the analysis results of the light curves at the position indicated by the turquoise line in Fig. 4. And the same period as about 90 s is detected again. As marked by the purple and turquoise lines, they are symmetrically located at two sides of the CBP core. The different peaks in Fig. 6 represent the various flows towards the northwest, while those in Fig. 7 are the flows towards the southeast. The same periods detected in them not only indicate the periodicity, but also further confirm the symmetrical property of the bi-directional flows.

### 4.2. The magnetic field

Fig. 8 shows the LOS magnetograms from HMI at four different times, which cover the entire lifetime of the CBP. Except for the positive and negative fields within the big region, which are stable before and after the CBP, there is a flashed positive field with a small region like  $4.8'' \times 7.2''$ , as marked by the blue box. The contours are set at 20 G. Fig. 9 (bottom) shows the time evolution of this positive field strength (black profiles). It seems to enhance at about 01:03 UT, and reach its maximum at about 01:06:30 UT, while almost disappear at around 01:08 UT. It has a lifetime of  $\sim 5$  minutes, which covers the CBP lifetime very well. The CBP takes place at the position be-

tween this flashed positive field and negative field. The plus marks the core where the CBP starts. Meanwhile, this positive field moves towards the negative field during the CBP lifetime.

Fig. 10 (bottom) shows the time-distance slice along a directional slit, as indicated by two white solid lines in Fig. 8. It is from 00:55 UT to 01:18 UT, which covers the CBP whole lifetime. Except for this positive field decreases its strength (as indicated by the contours), it moves close towards the negative field with a stable speed of about  $1.2 \text{ km s}^{-1}$  (blue arrow). Actually, the negative field also moves close to the positive field at a speed of around  $2.6 \text{ km s}^{-1}$  (red arrow), then stops after the CBP maximum. These facts suggest the magnetic cancellation occurrence at the position of the CBP core. Our findings are agreement very well with previous results about the relationship between the CBPs and magnetic fields (e.g., Golub et al. 1976; Harvey 1985; Webb et al. 1993; Li & Ning 2012; Zhang et al. 2012; Chen et al. 2015). All these studies found that the CBPs were related to the small-scale magnetic fields, especially the magnetic dipoles. Which means that the CBPs are originating from the small-scale magnetic reconnections.

#### 4.3. The DEM analysis

In order to investigate the temperature and emission measure (EM) of the CBP, we perform the DEM analysis using the six AIA EUV bands, such as 94 Å, 131 Å, 171 Å, 193 Å, 211 Å, and 335 Å (Cheng et al. 2012). Firstly, we have to measure their fluxes at the small regions, such as p1, p2 and p3 labeled in Fig. 3. The region of p2 is located at the CBP core, while p1 and p3 regions are outside of the CBP. Then the function of the DEM dependence on the temperature is fitting from the observations. Fig. 11 shows the DEM curves of the p2 region at four times. The best-fit DEM solution to the observed fluxes are indicated with the black solid profiles. And the 100 Monte Carlo (MC) realizations of the data are computed to estimate the DEM uncertainties, as indicated by the color rectangles. The yellow rectangles represent the region surrounding the best-fit solution that contains 50% of the MC solutions, and two turquoise and one yellow rectangles are consisted of the regions that covers 80% of the MC solutions, while all of the colored rectangles include

the regions which contain 95% of the MC solutions. Therefore, the top and bottom ends of the colored rectangles can be regarded as the uncertainties of the DEM analysis. Given the uncertainties of the DEM analysis, the average temperature ( $T$ ) and emission measure (EM) at each time are calculated over the temperature range from  $\log T = 5.7$  to  $\log T = 7.0$ .

Fig. 12 shows the time evolution of the average temperature (top) and EM (bottom) at three regions of p1, p2 and p3. The CBP core (p2) increases its temperature firstly (at  $\sim 01:03$  UT) and rapidly, while the p1 and p3 regions increase their temperature about 2 minutes later, at around 01:05 UT. This is consistent with the moving structures from the CBP core towards two sides. Similarly for the EM, p1 and p3 regions reach their peak values after the CBP core (p2), and the peak EM at the CBP core is almost at the same time as the AIA 171 Å maximum brightness (blue profile). The maximum values of both temperature and EM are at the CBP core region, and their values are about 3.148 MK and  $9.79 \times 10^{27} \text{ cm}^{-5}$ , which are in agreement with previous findings in the CBPs (e.g., Nolte et al. 1979; Tian et al. 2008a; Kariyappa et al. 2011; Hong et al. 2014; Zhang & Ji 2014b; Zhang et al. 2016). This DEM result is also consistent with the CBP behaviors at the various solar atmospheres. That is to say, the CBP can radiate stronger emissions at AIA 171 Å, 193 Å, 211 Å, 131 Å, 304 Å and SJI 1330 Å, 1400 Å, all these bands can detect the emissions from upper chromosphere, transition region or corona (quiet and active) at solar surface, which correspond the temperature of around 0.1–1.0 MK. But it radiates the weak emissions at AIA 94 and 335 Å, because these two bands mainly detect the emissions from the flaring corona which have a higher temperature. And it has nearly no radiations at AIA 1600 Å, 1700 Å and SJI 2796 Å, whose emissions are mostly from the photosphere or lower chromosphere, and have a lower temperature (below  $10^4 \text{ K}$ ). All these findings indicate that the CBP has a multi-temperature structures (see also., Fig. 11).

#### 5. Conclusions and Discussions

Based on the observations from *IRIS* and *SDO*, we explore the bi-directional moving structures in

a CBP at multi-bands, i.e., 7 AIA EUV and 2 SJI FUV bands. This CBP takes place at NOAA 12384 with a curved shape. AIA and SJI observations show that the CBP is brightening at AIA EUV and SJI FUV wavelengths. Meanwhile, the observations with high temporal resolution show that there are many bright structures moving intermittently from the CBP core outward two sides. From the time-distance slices along a curved slit, these moving structure are identified as the bi-directional flows toward northwest and southeast simultaneously. They display the similar shape and velocity, but opposite directions, and their average moving speed is around  $300 \text{ km s}^{-1}$ . They also show a typical periodicity with a quasi-period of  $\sim 90 \text{ s}$ .

In our results, at least two pairs of bi-directional flows are detected simultaneously at all the 9 wavelengths from AIA and SJI observations, as indicated by the purple and blue arrows in Fig. 5. This finding fills the gap that the bi-directional flows are not observed simultaneously at all 9 AIA wavelengths (Ning & Guo 2014). Here, we use the observations from SJI FUV images instead of AIA UV images. This is because the CBP has very weak radiations at AIA UV bands (see., Fig. 2). Thus, the bi-directional flows induced by the instrument self-effects can also be ruled out, since observations are from two different instruments which onboard *SDO* and *IRIS*, respectively. And the quasi-period of  $\sim 90 \text{ s}$  are also detected simultaneously at all these 9 wavelengths at the symmetrical positions from the CBP core (see., Fig. 6 and 7), suggesting the quasi-periodic oscillations in this CBP. This is similar as previous findings (e.g., Nolte et al. 1979; Tian et al. 2008b; Ning & Guo 2014; Zhang & Ji 2014a; Samanta et al. 2015), and maybe related with the reciprocity magnetic reconnection (e.g., Priest et al. 1994; Zhang et al. 2014; Chen et al. 2015). The period could be modulated by certain MHD wave (Chen & Priest 2006; Banerjee & Krishna Prasad 2016). The simultaneous, symmetry and quasi-periodic bi-directional flows in a CBP can be detected at all the 9 wavelengths, suggesting that the flows could be existed at various solar atmosphere layers. For example, the chromosphere and transition region (AIA 131 and  $304 \text{ \AA}$ , SJI 1330 and  $1400 \text{ \AA}$ ), the quiet corona (AIA  $171 \text{ \AA}$ ), the active-region corona (AIA 193,

211 and  $335 \text{ \AA}$ ), and even the flaring corona (AIA 94, 131, and  $193 \text{ \AA}$ ) (Lemen et al. 2012; De Pontieu et al. 2014). There are much less and weaker flows detected at AIA 94 and  $335 \text{ \AA}$  (Fig. 4 and 5), indicating that the flows mainly behaving at the transition region and corona, further suggesting that the temperature of the CBP is around  $1.0 \text{ MK}$ , which is similar to the DEM analysis results (see., Fig. 11 and 12). This is also consistent with previous findings about the study of CBP temperature (Nolte et al. 1979; Tian et al. 2008a; Kariyappa et al. 2011; Zhang & Ji 2014b).

The average velocity of these bi-directional flows is around  $300 \text{ km s}^{-1}$  (see., Fig. 5), this value has the same order of the outflows which detected in the solar flares (e.g., Wang et al. 2007; Li & Zhang 2009; Liu et al. 2013; Su et al. 2013; Young et al. 2013; Ning 2016). On the other hand, statistical results find that the CBPs and solar flares display the similar power-law behaviors, and the power-law index is closing to 2.0 (e.g., Dennis 1985; Crosby et al. 1993; Aschwanden et al. 1998; Li et al. 2013). All these similar findings between the CBPs and solar flares suggest that there is no fundamental difference to generate them. Researches further indicate that they are strongly related to the magnetic structures (small or large scales) at the solar surface. In other words, the mechanisms of the magnetic features which related to the solar eruptions (CBPs and solar flares) on solar disk are scale-free (see also., Parnell et al. 2009).

HMI observations show that a flashed positive field emerges near the CBP core (Fig. 8). And it has a short lifetime, same as the CBP interval. Meanwhile, it moves close towards the nearby negative field, and this CBP takes place between them (Fig. 9 and 10). Furthermore, the CBP core increases its temperature and emission measure earlier than the outside regions (Fig. 12). All these facts support that the magnetic reconnection model can explain this CBP and the bi-directional flows. It is well known that the magnetic reconnection is the basic process which the magnetic energy convert into kinetic energy at the solar atmosphere (Innes et al. 1997). And this magnetic reconnection model has been used to explain the solar eruptions in various scales, such as the solar flares and CMEs in large scale (Su et al. 2013; Liu et al. 2013; Li et al. 2015; Ning 2016), CBPs and transi-

tion explosive events in small scale (Pérez et al. 1999; Zhang et al. 2012; Innes & Teriaca 2013; Ning & Guo 2014; Innes et al. 2015). However, the direct observation evidences which support the magnetic reconnection are rare, because of the lower spatial and temporal resolution observations. Innes et al. (1997) had indicated that the bi-directional outflows in the transition explosive events can be as the direct observational evidence of the magnetic reconnection. This is consistent with the MHD results, which suggest that the bi-directional outflows in the explosive events are from magnetic reconnection regions (Innes & Tóth 1999; Sarro et al. 1999; Roussev et al. 2001a,b). Recently, Ning & Guo (2014) detected the similar bi-directional outflows in a CBP, and considered them as the direct observational evidence of the magnetic reconnection. Therefore, the bi-directional flows in this CBP could be the bi-directional outflows, and they can be as the direct observation evidence of the magnetic reconnection at solar surface. Considering the radiations from this CBP are mainly from the transition region and lower corona, together with the statistical results that there are hundreds of CBPs emergence at solar surface at any given time (Zhang et al. 2001), they could be contributed to the coronal heating (Priest et al. 1994).

In this paper, we report the bi-directional outflows and their quasi-periodicity in a CBP observed at by *SDO*/AIA and *IRIS*/SJI. They could be explained by the reconnection model. This is similar as the bi-directional outflows in the explosive events which also interpreted as the reconnection jets (e.g., Innes et al. 1997; Innes & Tóth 1999; Sarro et al. 1999; Pérez et al. 1999; Roussev et al. 2001a,b; Innes & Teriaca 2013; Innes et al. 2015). As indicated by Chae et al. (1998), the explosive events may be the manifestation of hot plasma materials flowing out of the transition region. Therefore, the outflows in this CBP could represent the hot plasmas flowing out of the solar atmospheres, including the upper chromosphere, transition region and lower corona. In other words, the bi-directional outflows in explosive events and CBPs may have the similar physical mechanism, but they display the different observational features at the spectral and imaging observations (see also., Chae et al. 2000). In future, the joint observations from the *IRIS*

spectra and *SDO* images could be a good topic to study their originations. The quasi-period of about 90 s may be modulated by some MHD waves (Chen & Priest 2006; Banerjee & Krishna Prasad 2016). However, it is hard to determine the MHD waves which could play the key effects here, because of the observation limits. Therefore, future work will also focus on the analysis of the wave-modulation causing the periodicity in CBPs or explosive events.

We would like to thank the anonymous referee for his/her valuable comments to improve the manuscript. The data used in this paper are mainly from *IRIS* and *SDO*. *IRIS* is a NASA small explorer mission developed and operated by LMSAL with mission operations executed at NASA Ames Research center and major contributions to downlink communications funded by the Norwegian Space Center (NSC, Norway) through an ESA PRODEX contract. *SDO* is the first mission to be launched under NASA's Living With a Star (LWS) program. This study is supported by NSFC under grants 11333009, 11303101, 11473071, 11573072, 973 program (2014CB744200) and Laboratory NO. 2010DP173032. This work is also supported by the Youth Fund of Jiangsu No. BK20141043, BK20161095, and one hundred talent program of Chinese Academy of Sciences.

## REFERENCES

- Alexander, C. E., Del Zanna, G., & Maclean, R. C. 2011, *A&A*, 526, A134
- Alipour, N., & Safari, H. 2015, *ApJ*, 807, 175
- Aschwanden, M. J., Dennis, B. R., & Benz, A. O. 1998, *ApJ*, 497, 972
- Banerjee, D., & Krishna Prasad, S. 2016, Washington DC American Geophysical Union Geophysical Monograph Series, 216, 419
- Brković, A., & Peter, H. 2004, *A&A*, 422, 709
- Bewsher, D., Innes, D. E., Parnell, C. E., & Brown, D. S. 2005, *A&A*, 432, 307
- Chae, J., Wang, H., Lee, C.-Y., Goode, P. R., & Schühle, U. 1998, *ApJ*, 504, L123

- Chae, J., Wang, H., Goode, P. R., Fludra, A., & Schühle, U. 2000, *ApJ*, 528, L119
- Chen, P. F., & Priest, E. R. 2006, *Sol. Phys.*, 238, 313
- Chen, J., Su, J., Yin, Z., et al. 2015, *ApJ*, 815, 71
- Cheng, X., Zhang, J., Saar, S. H., & Ding, M. D. 2012, *ApJ*, 761, 62
- Crosby, N. B., Aschwanden, M. J., & Dennis, B. R. 1993, *Sol. Phys.*, 143, 275
- Dennis, B. R. 1985, *Sol. Phys.*, 100, 465
- De Pontieu, B., & Title, A. M., & Lemen, J. R., et al. 2014, *Sol. Phys.*, 289, 2733
- Golub, L., Krieger, A. S., Silk, J. K., Timothy, A. F., & Vaiana, G. S. 1974, *ApJ*, 189, L93
- Golub, L., Krieger, A. S., & Vaiana, G. S. 1976, *Sol. Phys.*, 50, 311
- Harvey, K. L. 1985, *Australian Journal of Physics*, 38, 875
- Harvey, K. L., Strong, K. S., Nitta, N., & Tsuneta, S. 1994, *Solar Active Region Evolution: Comparing Models with Observations*, 68, 377
- Hong, J., Jiang, Y., Yang, J., et al. 2014, *ApJ*, 796, 73
- Innes, D. E., Inhester, B., Axford, W. I., & Wilhelm, K. 1997, *Nature*, 386, 811
- Innes, D. E., & Tóth, G. 1999, *Sol. Phys.*, 185, 127
- Innes, D. E., & Teriaca, L. 2013, *Sol. Phys.*, 282, 453
- Innes, D. E., Guo, L.-J., Huang, Y.-M., & Bhattacharjee, A. 2015, *ApJ*, 813, 86
- Kariyappa, R., Deluca, E. E., Saar, S. H., et al. 2011, *A&A*, 526, A78
- Lemen, J. R., & Title, A. M., & Akin, D. J., et al. 2012, *Sol. Phys.*, 275, 17
- Li, L., & Zhang, J. 2009, *ApJ*, 703, 877
- Li, D., & Ning, Z. 2012, *Ap&SS*, 341, 215
- Li, D., Ning, Z. J., & Wang, J. F. 2013, *New A*, 23, 19
- Li, D., Ning, Z. J., & Zhang, Q. M. 2015, *ApJ*, 807, 72
- Liu, W., Chen, Q., & Petrosian, V. 2013, *ApJ*, 767, 168
- Ning, Z., Cao, W., & Goode, P. R. 2009a, *ApJ*, 707, 1124
- Ning, Z., Cao, W., Okamoto, T. J., Ichimoto, K., & Qu, Z. Q. 2009b, *A&A*, 499, 595
- Ning, Z., & Guo, Y. 2014, *ApJ*, 794, 79
- Ning, Z. 2016, *Ap&SS*, 361, 22
- Nolte, J. T., Solodyna, C. V., & Gerassimenko, M. 1979, *Sol. Phys.*, 63, 113
- Parnell, C. E., DeForest, C. E., Hagenaar, H. J., et al. 2009, *ApJ*, 698, 75
- Pérez, M. E., Doyle, J. G., Erdélyi, R., & Sarro, L. M. 1999, *A&A*, 342, 279
- Priest, E. R., Parnell, C. E., & Martin, S. F. 1994, *ApJ*, 427, 459
- Roussev, I., Galsgaard, K., Erdélyi, R., & Doyle, J. G. 2001a, *A&A*, 370, 298
- Roussev, I., Doyle, J. G., Galsgaard, K., & Erdélyi, R. 2001b, *A&A*, 380, 719
- Samanta, T., Banerjee, D., & Tian, H. 2015, *ApJ*, 806, 172
- Sarro, L. M., Erdélyi, R., Doyle, J. G., & Pérez, M. E. 1999, *A&A*, 351, 721
- Schou, J., & Scherrer, P. H., & Bush, R. I., et al. 2012, *Sol. Phys.*, 275, 229
- Sturrock, P. A., & Coppi, B. 1964, *Nature*, 204, 61
- Su, Y., Veronig, A. M., Holman, G. D., et al. 2013, *Nature Physics*, 9, 489
- Tian, H., Curdt, W., Marsch, E., & He, J. 2008a, *ApJ*, 681, L121
- Tian, H., Xia, L.-D., & Li, S. 2008b, *A&A*, 489, 741
- Vaiana, G. S., Davis, J. M., Giacconi, R., et al. 1973, *ApJ*, 185, L47



- Wang, T., Sui, L., & Qiu, J. 2007, ApJ, 661, L207
- Webb, D. F., Martin, S. F., Moses, D., & Harvey, J. W. 1993, Sol. Phys., 144, 15
- Wilhelm, K., Lemaire, P., Curdt, W., et al. 1997, Sol. Phys., 170, 75
- Young, P. R., Doschek, G. A., Warren, H. P., & Hara, H. 2013, ApJ, 766, 127
- Zhang, Q. M., Chen, P. F., Guo, Y., Fang, C., & Ding, M. D. 2012, ApJ, 746, 19
- Zhang, Q. M., & Ji, H. S. 2013, A&A, 557, L5
- Zhang, Q. M., Chen, P. F., Ding, M. D., & Ji, H. S. 2014, A&A, 568, A30
- Zhang, Q. M., & Ji, H. S. 2014a, A&A, 561, A134
- Zhang, Q. M., & Ji, H. S. 2014b, A&A, 567, A11
- Zhang, Q. M., Ji, H. S., & Su, Y. N. 2016, Sol. Phys., 291, 859
- Zhang, J., Kundu, M. R., & White, S. M. 2001, Sol. Phys., 198, 347

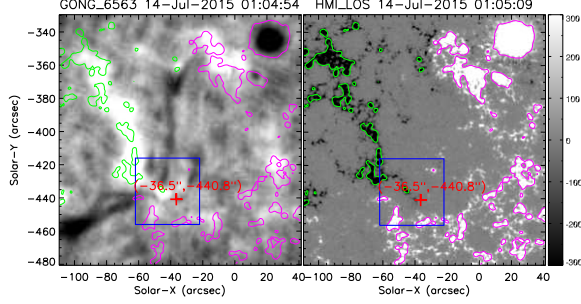


Fig. 1.—  $H\alpha$  6563 Å image (left) from NSO/GONG, and LOS magnetogram (right) from SDO/HMI. The contours represent the magnetic fields at the levels of 200 (purple) and -200 (green) G, respectively. The blue box marks the region in Fig. 2, and the red plus (+) indicates the CBP core.

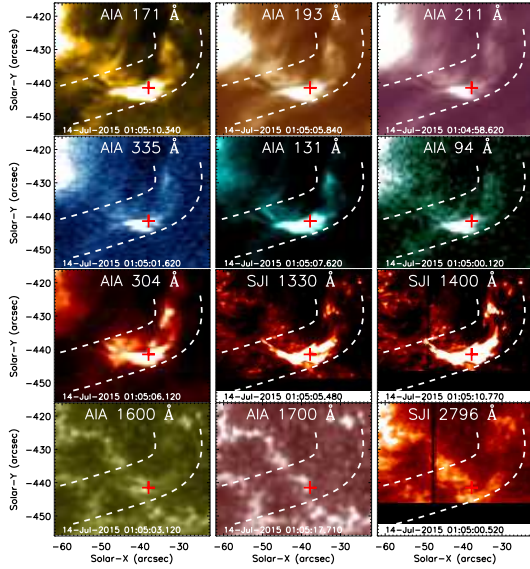


Fig. 2.— The CBP at SDO/AIA and IRIS/SJI images. Two dashed curves outline the curved slit where the CBP takes place. The red plus (+) marks the CBP core.

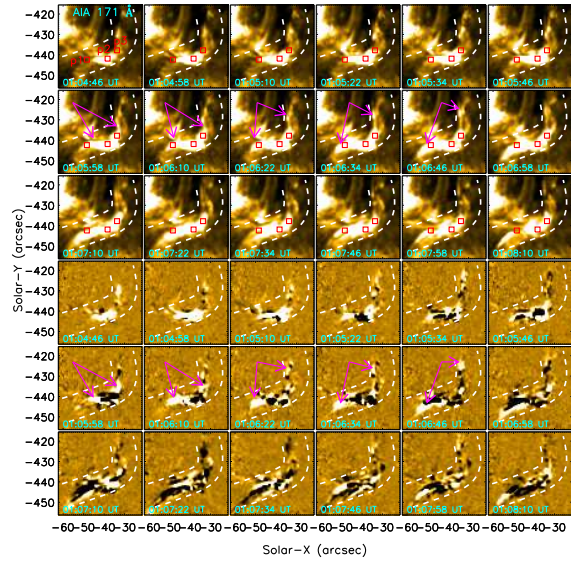


Fig. 3.— Time sequence of AIA 171 Å images (the top 18 panels) and their running-difference images (the bottom 18 panels). Each image has the same size of  $40'' \times 40''$ . Two dashed curves outline the curved slit. The three red boxes indicate the regions ( $2.4'' \times 2.4''$ ) used to do the DEM analysis in Fig. 11. The purple arrows mark a pair of the moving structures (flows).

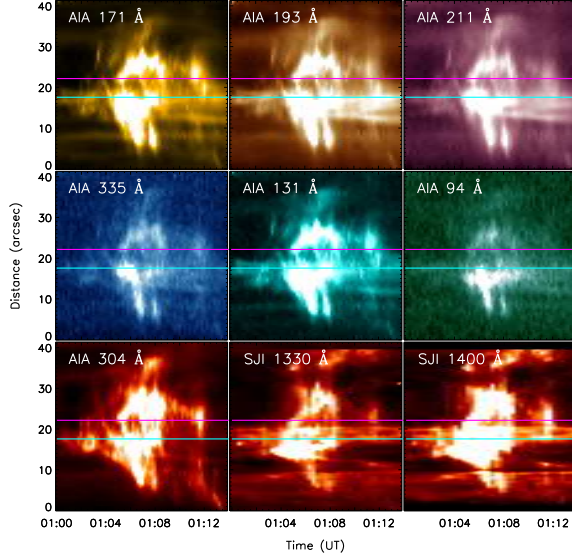


Fig. 4.— Time-distance slices at 7 AIA EUV bands and 2 SJI wavelengths along the curved slit in Fig. 2. The purple and turquoise lines indicate the two symmetrical positions whose light curves are studied in Fig. 6 and Fig. 7.

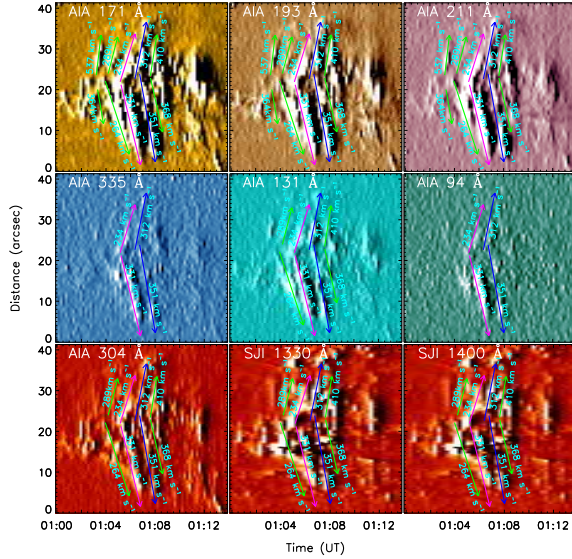


Fig. 5.— Derivative (gradient along the time axis) of the time-distance slice in Fig. 4. The arrows mark the various pairs of the moving structures (flows).

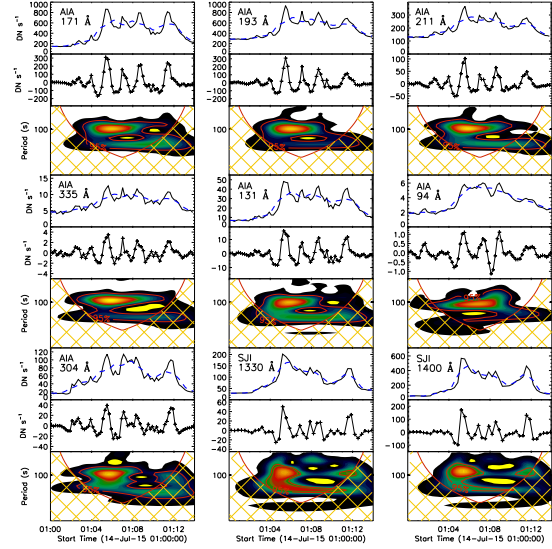


Fig. 6.— Wavelet analysis of the light curves at 9 wavelengths. Top: light curves (solid) with the slowly varying components (dashed) at the position marked by the purple line in Fig. 4. Middle: the rapidly varying components (plus). Bottom: wavelet spectra.

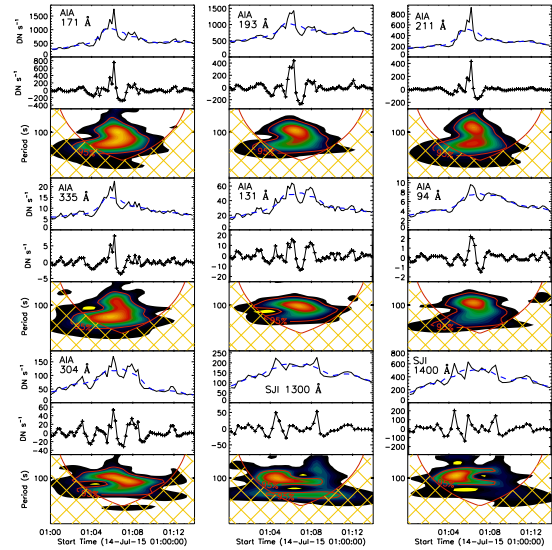


Fig. 7.— Same as Fig. 6, but the analysis is performed at the position marked by the turquoise lines in Fig. 4.

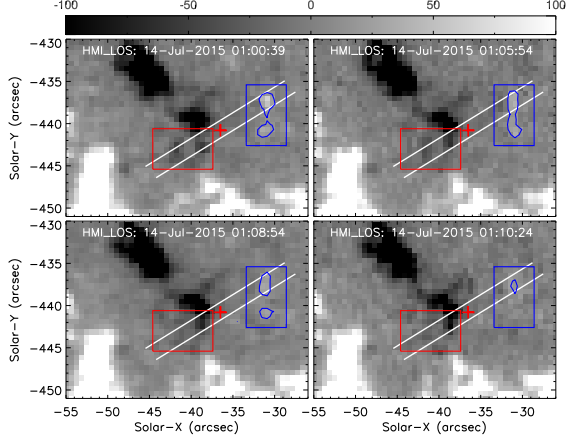


Fig. 8.— HMI magnetograms at four times. The contours represent the positive fields at the levels of 20 G. Each image has the same size of  $29'' \times 21''$ . Two solid lines outline the slit used in Fig. 10. The plus (+) indicates the CBP core. The rectangles mark the regions used to calculate the magnetic strength of positive (blue) and negative (red) fields.

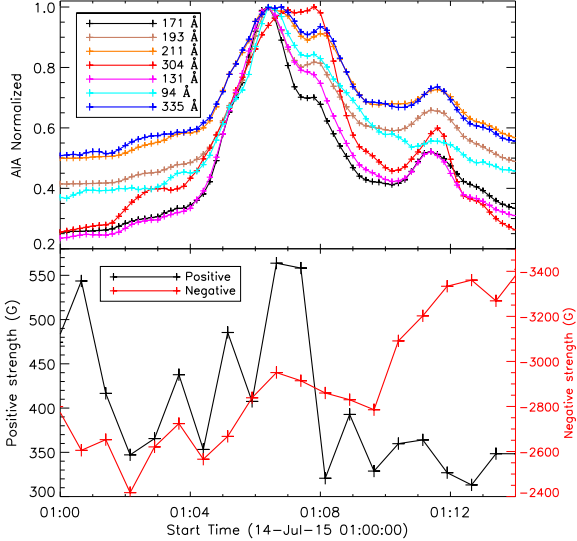


Fig. 9.— Top: the normalized light curves along the curved slice at 7 AIA EUV channels. Bottom: HMI magnetic field strength at the rectangle regions in Fig. 8.

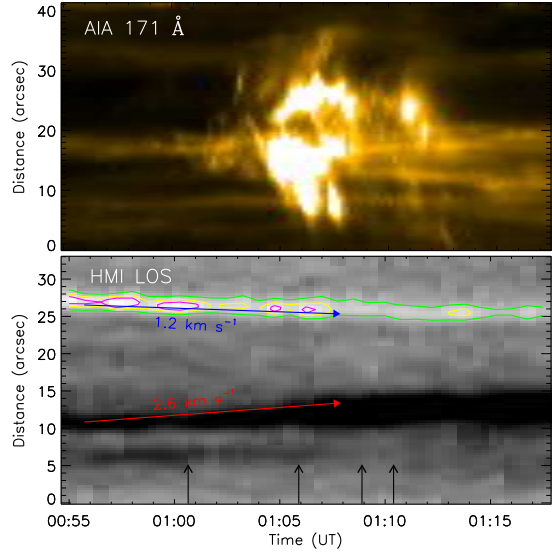


Fig. 10.— Top: Time-distance slice at AIA 171 Å along the curved slit in Fig. 2. Bottom: Time-distance slice along the tilt slit in Fig. 8. The contours represent the positive fields at the level of 55 G (green), 95 G (yellow) and 120 G (purple), respectively. The color arrows mark the movement of the positive (blue) and negative (red) magnetic fields, respectively. HMI images at four times marked by the black arrows are given in Fig. 8

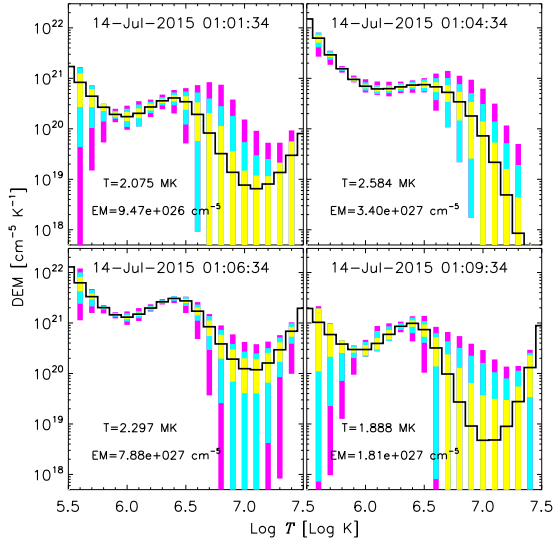


Fig. 11.— The DEM profiles of the CBP core (p2) at four times. The black solid profiles give the best-fitted DEM curves from the observations. The yellow rectangles represent the regions that contains 50% of the MC solutions. The turquoise rectangles, above and below the yellow rectangles, and the yellow rectangles compose the regions that cover 80% of the MC solutions. All of the colored rectangles form the regions containing 95% of the MC solutions. The average temperature and EM are given.

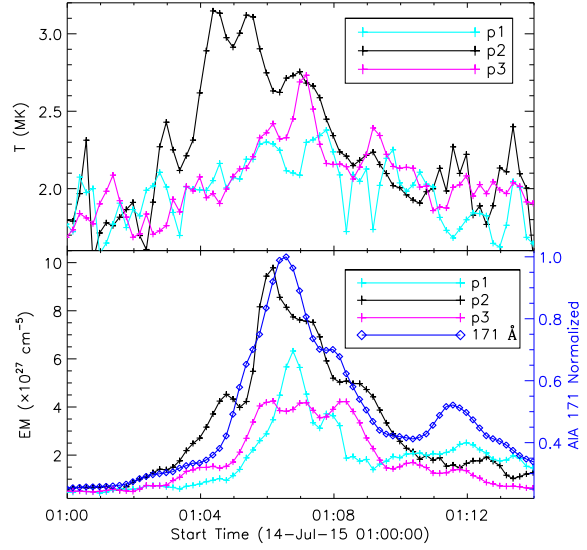


Fig. 12.— The light curves of the temperature (top) and EM (bottom) from the DEM analysis at three regions of p1, p2 and p3. The 171 normalized flux (blue) is given.